Composites Part B 301 (2025) 112513

Contents lists available at ScienceDirect

Composites Part B

journal homepage: www.elsevier.com/locate/compositesb

# Improving energy absorption in cellular 3D-Printed fiber–reinforced structures with radially reinforced composite shells

Bence Szederkényi [a], Norbert K. Kovács [a,b], Tibor Czigany [a,c,*]

[a] Department of Polymer Engineering, Faculty of Mechanical Engineering, Budapest University of Technology and Economics, Muegyetem rkp. 3., H-1111, Budapest, Hungary
[b] MTA-BME Lendület Lightweight Polymer Composites Research Group, Muegyetem rkp. 3., H-1111, Budapest, Hungary
[c] HUN-REN-BME Research Group for Composite Science and Technology, Muegyetem rkp. 3., H-1111, Budapest, Hungary

ARTICLE INFO

Handling Editor: Prof. Ole Thomsen

*Keywords:*
3D printed carbon fiber–reinforced polymer
Cellular structures
Triply periodic minimal surfaces
Energy absorption
Specific energy absorption
Shell reinforcement

ABSTRACT

This study investigates the energy absorption capabilities of cellular structures combined with carbon fiber–reinforced polymer shells. The cellular core was produced by material extrusion 3D printing, while the shells were manufactured by the hand layup of carbon fiber-epoxy prepreg. Various material and reinforcement configurations were analyzed in a combined configuration and separately on a component level. The energy absorption properties of the printed specimens were evaluated after quasi-dynamic compression tests, demonstrating that the introduced radially reinforced hoop layers significantly improved compressive load-bearing capacity by resisting delamination and, consequently, local buckling in the 3D-printed cellular structures. This led to stable failure modes and higher specific energy absorption (SEA). The hybrid structures, which combined external shells with a cellular framework, exhibited a synergistic effect, resulting in up to a 200 % improvement in SEA.

## 1. Introduction

Energy-absorbing materials and structures play a critical role in mitigating dynamic impacts. Materials and structures used in crashworthiness applications can dissipate energy through controlled structural deformation, thereby significantly reducing peak loads on the objects they are designed to protect [1]. The design of impact attenuators is governed by several key parameters, including the maximum tolerable force, deceleration limits, and structural stability under dynamic conditions [2]. Conventional energy-absorbing materials have been widely used in crashworthiness engineering due to their effectiveness in absorbing impact energy. These materials include various polymers and metals, especially in foams or cellular configurations. Polymers and metals mainly absorb energy through plastic deformation, which causes their cellular configurations to behave predictably as the cell walls gradually collapse. These materials are preferred in several applications as they are lightweight, easy to produce, and have tunable energy absorption capacity. Tomin et al. [3] showed the adaptability of polymer foams in sports applications by exploiting their tunable porosity to enhance energy absorption. Similarly, Orbulov et al. [4] underscored the benefits of metal composite foams, emphasizing that they are lightweight yet robust, making them particularly suitable for transportation applications.

Composite materials have led to significant improvements in energy absorption devices, particularly in applications that demand higher performance than metals or unreinforced polymers. Starbuck et al. [5] emphasized the role of fiber failure and crack propagation as primary energy dissipation mechanisms in composites. Heimbs and Strobl [6] thoroughly investigated the crash behavior of composites in high-energy applications such as Formula 1 racing, while Boria et al. [7] and Kohlgrueber and Kamoulakos [8] examined the effectiveness of composite crash structures in the field of automotive and aerospace sectors. These studies emphasize the advantages of composites, such as high specific energy absorption (SEA) as a result of tailored failure modes, which make them highly advantageous in crashworthiness applications.

Homogeneous materials and spatially uniform structures, such as foams and honeycombs, represent the current generation of energy-absorbing designs in commercial applications. Despite their advantages, they have inherent limitations, such as lack of spatial tunability and isotropic mechanical response. These limit their use in applications

* Corresponding author. Department of Polymer Engineering, Faculty of Mechanical Engineering, Budapest University of Technology and Economics, Muegyetem rkp. 3., H-1111, Budapest, Hungary.
*E-mail address:* czigany@eik.bme.hu (T. Czigany).

https://doi.org/10.1016/j.compositesb.2025.112513
Received 20 January 2025; Received in revised form 26 March 2025; Accepted 8 April 2025
Available online 9 April 2025
1359-8368/© 2025 The Authors. Published by Elsevier Ltd. This is an open access article under the CC BY license (http://creativecommons.org/licenses/by/4.0/).

requiring a high degree of customization. Additive manufacturing (AM) is capable of producing novel cellular structures, which afford greater control over geometric parameters such as relative density spatially varying cell size and wall thickness. Among cellular structures particularly suitable for 3D printing, triple periodic minimal surfaces (TPMS) have gained considerable attention due to their unique geometric properties. TPMS structures are continuous, joint-free surfaces that distribute stress uniformly and are highly suitable for energy absorption. Studies such as those by Abueidda et al. [9,10] have demonstrated the superior mechanical performance of TPMS lattices, with gyroid structures exhibiting exceptional energy absorption and stress distribution. Sood and Wu [11] demonstrated that the dynamic behavior of brittle polymers is highly influenced by their 3D-printed configuration, offering tunable energy absorption based on printing parameters. Kladovasilakis et al. [12] and Sathishkumar et al. [13] highlighted the influence of design parameters such as unit cell size and relative density on energy absorption. The introduction of graded or functionally tunable TPMS designs has increased the potential of these structures in energy absorption applications. Qiu et al. [14] investigated functionally graded TPMS structures, showing their optimized mechanical behavior under multidirectional loading. Santiago et al. [15] extended this concept to high strain-rate impacts, achieving significant improvements in SEA by fine-tuning lattice designs. Additionally, Alduais and Özerinç [16] demonstrated that the mechanical properties of thermoplastic foams can be effectively tuned through manufacturing process parameters. They managed to adjust strength and density by controlled foaming mechanisms. These innovations show the versatility of TPMS and cellular structures produced by AM, and extend their application range in crashworthiness applications.

Combining the advantages of composites with the locally adjustable properties of TPMS structures makes it possible to create structures with better and tunable energy absorption. Carbon fiber–reinforced polymer (CFRP) crash zones, commonly used in high-performance crash boxes, are typically thin-walled, highly anisotropic structures, with considerably worse performance in lateral loading conditions. While 3D-printed TPMS structures theoretically provide a more isotropic behavior, extrusion-based technologies have weak interlayer adhesion and are therefore more prone to premature failure by delamination [11]. While thin-walled shell structures and 3D-printed lattices have the above issues, these can be mitigated with the appropriate hybrid configurations. Bhudolia et al. [17] demonstrated the benefits of hybrid thermoplastic composites under dynamic loading, and studies on aluminum/CFRP composite tubes have shown improved impact resistance under various conditions [18].

The primary objective of this study is to create hybrid, fiber-reinforced cellular structures that can efficiently absorb energy through controlled, progressive failure mechanisms. Drawing from the existing literature, the present study concentrates on hybrid energy-absorbing structures that integrate 3D-printed TPMS geometries reinforced with carbon fiber–epoxy prepreg hoop layers. The shell structure has been designed to address the shortcomings of previous configurations [19], in which premature, delamination-dominated failure modes were observed due to weak interlayer adhesion and, therefore, poor resistance to radial forces from axial compression. The study systematically compares the performance of these hybrid designs with that of their components, showing the synergistic benefits of combining 3D-printed TPMS structures with composite shells.

## 2. Methodology

In the tests, three main types of components were used: TPMS structures 3D printed from a thermoplastic material, the same structures reinforced with continuous carbon fiber, and shell structures made from CF–reinforced epoxy prepreg. The hybrid structures were created by combining the shell and TPMS components. The specimens were subjected to quasi-dynamic compression tests, and the results were compared based on the energy absorbed. The following sections present the construction of these individual components, the methods with which the hybrid systems were tested, and the metrics used to compare them.

### 2.1. Materials used

Three material combinations with distinct failure behaviors were used to validate the shell-reinforcing hypothesis. Markforged Nylon White (PA6) and Onyx (short carbon fiber–reinforced PA6) were selected in the first step due to their pronounced plastic behavior and highly non-linear stress–strain response. These materials show significant deformation before failure, so they are suitable for assessing the reinforcing effect under non-brittle failure conditions. Both were reinforced with 1k carbon fiber strands produced by Markforged.

A 4043D monomer-based PLA from Herz Hungary was introduced to improve manufacturing efficiency. PLA allowed faster and more stable production with lower sensitivity to temperature fluctuations, while reducing anisotropy. Unlike PA6 and Onyx, PLA has a more linear stress–strain response and fails in a brittle manner. This makes it an ideal contrasting material in the study. While PLA specimens did not receive additional reinforcement, they were retained in the test series as a control group, providing a cost-effective and rapidly producible reference for comparison. This dual-material approach—brittle and pseudoplastic—ensured a comprehensive validation of the reinforcing concept.

### 2.2. Preparation of specimens

#### 2.2.1. Internal cellular structure

In this study, cylindrical specimens with a diameter of 43.5 mm and a height of 50 mm were used due to concerns regarding the manufacturability of the prepreg shell. The specimens were printed in a specific orientation, XY and Z. XY specimens were printed in a laying orientation, and Z specimens were printed in a standing orientation (Fig. 1).

TPMS cell structures were selected based on three criteria: (i) feasibility of support-free manufacturing with material extrusion (MEX) technology, (ii) the presence of elongated, uninterrupted cross-sections perpendicular to the primary build direction to facilitate continuous fiber placement, and (iii) geometric optimization for enhanced energy absorption. Building upon our previous research [19] and the findings of Kladovasilakis et al. [12] and Saleh et al. [20], the investigation focused exclusively on the Schwarz-Diamond cell (Fig. 2 (a)). This structure was selected because it has superior specific energy absorption (SEA) properties and is suitable for reinforcement in a CFR 3D printing environment, due to its periodically repeating, strut-like cross-sections (Fig. 2(b and c)).

According to literature recommendations, we aligned unit cells in the

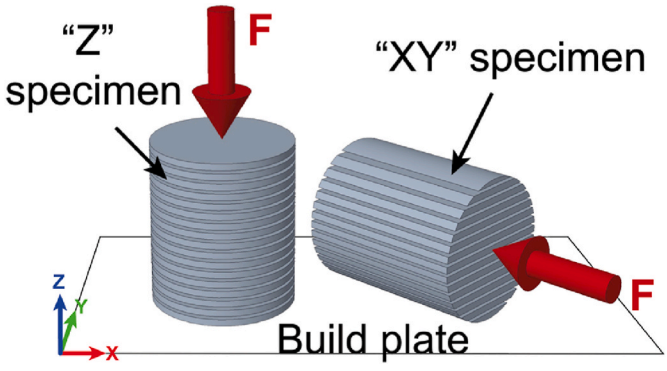


**Fig. 1.** The build orientation of the specimens on the printing platform, and the corresponding loading directions (red arrows) had a consistent axial alignment irrespective of the printing directions.

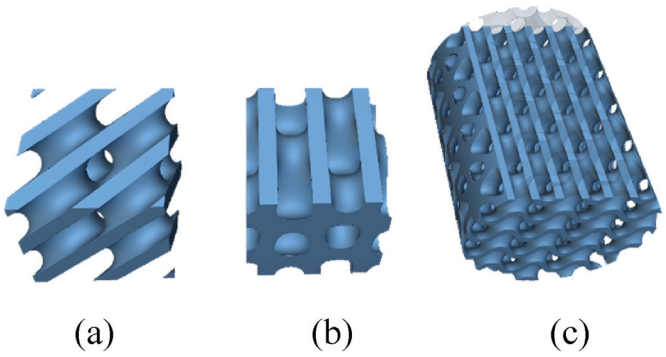


**Fig. 2.** The representative Schwarz-Diamond TPMS cell (a), its 45° rotated configuration (b), and the geometry of the specimen used for the compression tests – the axially reinforced cross-sections of one of the specimens (c).

vertical direction with a 15 mm edge length; at least 3 unit cells in one direction are recommended to mitigate edge effects [21]. The characteristic edge length was primarily determined by the narrowest fiber-reinforced cross-section, which was 2.8 mm, based on both literature data [22] and the authors' previous measurements. As a result, the compression-tested cylinder had a relative density of 37.3 %. Table 1 contains the geometric properties of the compression specimens.

#### 2.2.2. Fiber reinforcement

*2.2.2.1. Radial reinforcement with external shells.* The shell structure integrates into the hybrid system. It provides resistance to radial forces induced by axial loading. At the same time, it minimizes its impact on the measured axial reaction forces. The tube-profiled shells were fabricated with 1-2-3 layers of unidirectional (UD) prepreg material. The crushing characteristics of these shells were examined in both standalone configurations and in combination with TPMS cellular systems.

The shells were produced from epoxy-prepreg. A 20 mm wide, 3 mm thick silicone tape was wound around a 40 mm diameter steel tube and then the layers were laminated onto it. The laminated layers were wrapped with an identical silicone band, which was tightened to the appropriate mechanical pressure. The completed piece was vacuum-bagged and cured in a T300 drying oven at 120 °C for 1.5 h without additional pressure, to enhance consolidation. Then, it was cut to size.

*2.2.2.2. Axial reinforcement with 3D-printed continuous fibers.* Stable and progressive failure processes in the fiber-reinforced regions are crucial for optimal energy absorption characteristics. There, the compression-dominated fibers should fragment into smaller pieces. Therefore, fibers were positioned parallel to the loading direction and confined to locations where the layers transitioned into straight, strut-like sections (Fig. 2(c)–. 3 (c)). This method ensured consistent reinforcement with uniform fiber orientation. For every 60 layers, eleven layers contained continuous fibers covering the entire cross-section. This configuration resulted in an approximate fiber content of 5 v% within the material-filled volume, assuming a fiber content of 37.4 % in the pre-impregnated strand, as reported by Lupone et al. [21]. For the fiber-reinforced TPMS structures, PA and Onyx materials were used. Table 2 contains the manufacturing properties of the compression specimens. Fig. 3 shows the schematic structure of an axially and radially–reinforced specimen.

**Table 1**
Geometric parameters of the compression specimens.

| | |
|---|---|
| Specimen nominal height | 50 mm |
| TPMS infill outer diameter | 43.5 mm |
| TPMS infill wall thickness | 2.8 mm |
| TPMS infill cell edge length | 15 mm |
| Shell (hoop) layer count | 1, 2 and 3 |
| Cured ply thickness | 0.23 mm |

A key hypothesis was that the local shape of reinforcement paths significantly influences the failure mechanism, as waviness in load-bearing struts is likely to induce bending-dominated failure. Higher curvature increases buckling length and reduces the number of fiber breakage points, potentially compromising structural integrity. To mitigate this effect, we designed specimens with fiber reinforcement columns as straight as the printer allowed (Fig. 3 (c)).

#### 2.2.3. Specimen combinations and assembly

In the tests, six basic specimen combinations were investigated (Fig. 4): the cellular structures were fabricated from the materials described in section 2.1. in either an upright (Z) or horizontal (XY) orientation, tested with both radial and axial fiber reinforcement. Axial fiber reinforcement was only investigated for the XY specimens, as it was not possible to produce the given configuration in the Z orientation. While the axial fiber reinforcement was added in one step during the printing of the TPMS structure, radial reinforcement was fabricated in a separate step and the components were pressed together with a tight fit without extra bonding applied.

## 3. Test environment and parameters

The quasi-dynamic compression tests were performed with a Zwick Z250 tensile testing machine at a loading speed of 600 mm/min at room temperature and 51 % relative humidity. The tests were performed up to 80 % of engineering deformation.

### 3.1. Comparative model

To ensure the comparability of the compression test results, we developed a model in which specimens were evaluated based on two primary metrics. Global performance was assessed with the use of specific energy absorption (SEA), while changes in relative performance were quantified with equations derived from the rule of mixtures (ROM). Although global metrics do not distinguish the contribution of individual components, the relationship between the performance of unreinforced and shell–reinforced specimens was established in proportion to the mass fractions of their components with a ROM-based approach. Since all specimens were compared according to SEA, the ROM-based metric was explicitly designed to isolate and highlight the reinforcing effect of the CFRP shell.

#### 3.1.1. Calculating specific energy absorption

SEA can be calculated with Equation (1) [22]:

$$SEA = \frac{\int_0^l F(x)dx}{m} \tag{1}$$

where $F(x)$ [N] is the force as a function of displacement $x$ [m], $m$ [g] is mass, and $l$ [m] is the stroke corresponding to the selected reference point for energy absorption evaluation. Thus, SEA is defined as the area under the force–displacement curve up to this reference point, normalized by the mass of the specimen. The calculation of SEA involves two distinct axes: the displacement domain, which defines the integration limit in Equation (1), and the force response, which governs the integral itself. The displacement-based component, represented by $l$ in Equation (1), indicates structural stability. At the same time, the force-based axis, defined by $F(x)$, reflects the structural properties, including material characteristics, cell topology, and instantaneous load-bearing capacity. To determine $l$, two approaches can be considered: a dynamic evaluation based on energy absorption efficiency and a static approach relying on the theoretical densification point. The dynamic approach identifies the stroke length using the energy absorption efficiency function introduced in Equation (2):

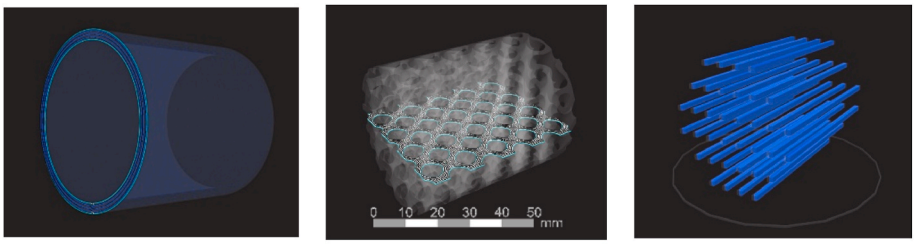


**Fig. 3.** Schematic representation of the 3D-printed axially reinforced specimens with external shell reinforcement: The structure has radially reinforced layers, manufactured separately from prepreg (a); an XY-oriented TPMS structure with 100 % concentric infill (b); and 3D-printed fiber reinforcement (c), which concentrically reinforces each strut with two parallel fiber bundles and is integrated into the structure during printing.

**Table 2**
Slicing parameters of the compression specimens.

| | |
|---|---|
| Layer thickness | 0.125 mm |
| Nozzle diameter | 0.4 mm |
| Infill ratio | 100 % |
| Wall count | 0 |
| Number of bottom/top layers | 0 |
| Reinforcement path planning | concentric, one-loop |
| Material deposition | concentric |

$$\eta(x) = \frac{\int_0^x F(x)dx}{F(x)\cdot x} \tag{2}$$

where η(x) [−] represents energy absorption efficiency, defined as the ratio of the absorbed energy up to a given deformation to the instantaneous force–displacement product at that deformation. Stroke length $l$ is then identified as the deformation at which η(x) reaches its maximum value, as expressed in Equation (3).

$$\eta(l) = \eta(x)|_{max}\ ;\ \frac{d\eta(x)}{dx} = 0 \tag{3}$$

where η(l) [−] represents the most efficient energy absorption point. Alternatively, a static SEA evaluation can be performed using a fixed stroke length based on the theoretical densification point derived from the structure's relative porosity. The densification strain $\epsilon_d$ is defined in Equation (5):

$$\epsilon_d = 1 - \rho^* \tag{5}$$

where $\rho^*$ [−] is the relative density of the cellular structure, the corresponding stroke length, $l_d$, is given by $l_d = \epsilon_d L$, where $L$ is the original specimen length. Substituting $l_d$ into Equation (1) allows SEA to be evaluated in a static manner, independent of deformation characteristics. Structural stability can be further assessed by comparing the static and dynamic SEA calculations. A significant discrepancy between $ld$ and $l$ suggests instability during deformation. In the reaction force domain, these instabilities appear as a reduction in the average plateau force, thereby lowering SEA values. The dynamic approach enhances sensitivity to these effects, as both stroke length and reaction force are used in the calculation of SEA.

While the static approach provides a reference based on material properties, it does not account for failure modes or local instabilities.

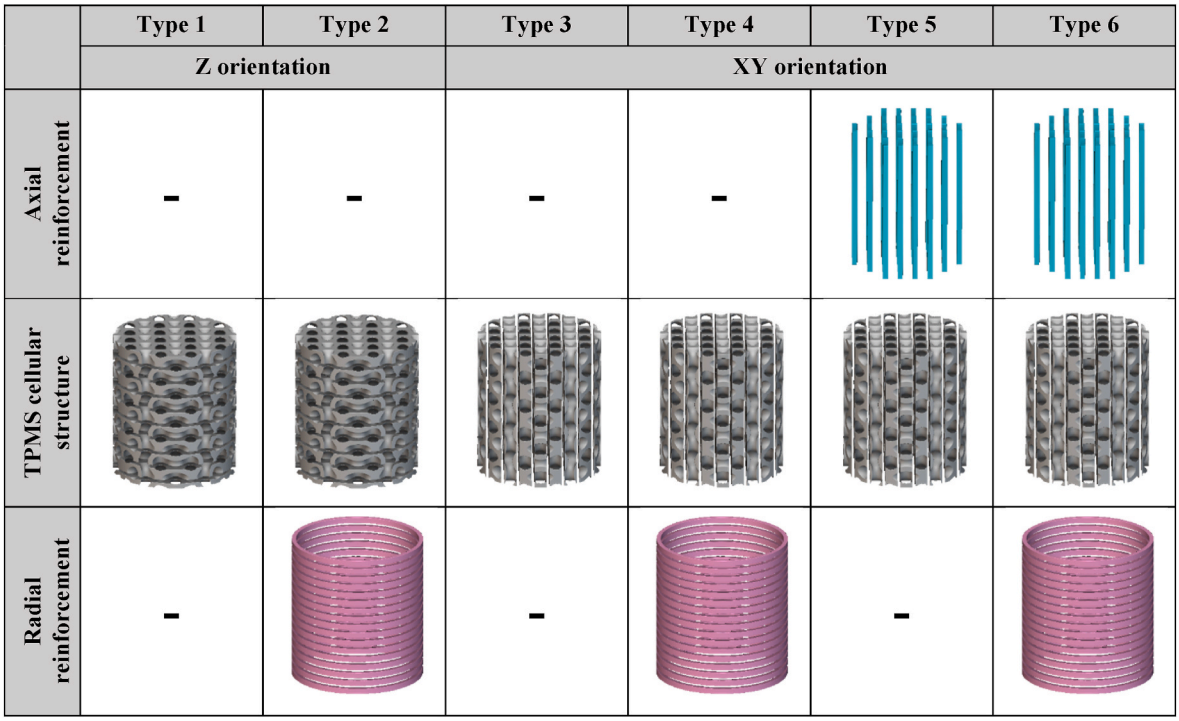


**Fig. 4.** The following schematic diagrams illustrate the specimen structures employed in the tests: the cellular structures are shown in grey, the axial 3D-printed fiber reinforcement in blue, and the radial prepreg hoop layers in pink.

The dynamic method, which better captures deformation behavior and structural instabilities, is the primary evaluation technique in this study, ensuring a more accurate assessment of energy absorption efficiency.

### 3.1.2. Rule of mixtures in energy absorption calculations

The rule of mixtures (ROM) can be applied to extensive state variables, such as energy absorption capability, to predict the combined performance of different structural components. We demonstrated and quantified the effect of coupling 3D-printed TPMS structures with CFRP shell reinforcements in this context. We calculated the specific energy absorption (SEA) of TPMS structures reinforced with hoop layers to analyze this interaction further. Moreover, to assess potential synergistic effects, we used the following approach: Let $SEA_{total}$ denote the energy absorption capability of the combined TPMS and shell structure, $SEA_{shell}$ the standalone energy absorption capability of the reinforced shell, and $SEA_{TPMS}$ the energy absorption capability of the TPMS structure. The masses are $m_{shell}$ for the external shell, $m_{TPMS}$ for the TPMS structure, and $m_{total}$ for the combined mass.

The mass fractions of the components can be defined as follows:

$$f_{shell} = \frac{m_{shell}}{m_{total}};\ f_{TPMS} = \frac{m_{TPMS}}{m_{total}} \tag{6}$$

$$m_{total} = m_{shell} + m_{TPMS} \tag{7}$$

$$f_{TPMS} + f_{shell} = 1 \tag{8}$$

Based on the first-order approximation using the rule of mixtures, the specific energy absorption capability of the entire structure can be expressed with Equation (9), assuming independent contributions from the TPMS and the shell.

$$SEA_{total,ROM} = f_{TPMS} * SEA_{TPMS,actual} + f_{shell} * SEA_{shell,actual} \tag{9}$$

where the subscript "*ROM*" refers to rule of mixtures–based predictions, while "*actual*" denotes experimentally obtained values from separately tested components. Then, using Equation (10), we compared the actual energy absorption capability of the hybrid TPMS structure reinforced with the shell ($SEA_{total,\ actual}$) to the SEA values proportional to the mass fractions of the components.

$$Synergy_{SEA} = \frac{SEA_{total,actual} - SEA_{total,ROM}}{SEA_{total,actual}} \cdot 100 \tag{10}$$

Synergy is confirmed when $Synergy_{SEA}$ exceeds 0 (expressed as a percentage). This approach allows the quantitative evaluation of the efficiency of the shell reinforcement and the synergistic potential of the hybrid structure. The difference in absolute energy absorption, normalized to mass (denoted by the subscript *abs.*), was determined with Equation (11). Here, the SEA increment achieved by shell reinforcement is expressed as a percentage—the hybrid structure is compared to its TPMS component.

$$\Delta SEA_{abs.} = \frac{SEA_{total,actual} - SEA_{TPMS,actual}}{SEA_{\ TPMS,actual}} \cdot 100 \tag{11}$$

## 4. Results and discussion

Table 3 contains the properties and names of the tested specimens. Fig. 5 shows the results of the compression in a bar chart. The load–displacement curves of the test specimens, sorted by orientation, base material, and reinforcement type, are shown in Figs. 6, 9 and 10. The compression graphs include the calculated densification point of the specimens, marked with a red X, along with their standard deviations.

Based on Equation (10) presented in Section 3.1.2, we prepared a bar chart showing the SEA of hybrid systems and their individual components (Fig. 5). Using Equations (10) and (11), we calculated the synergistic effect and the absolute difference in SEA. Table 4 contains the results. The resulting scatter values were obtained as the aggregated values of error propagation calculations performed directly on the measured SEA values.

### 4.1. Effect of hoop layer count in the shell structure

Individual shell samples were first tested for each layer count. This way, we determined the number of layers required to effectively reinforce the tested TPMS structure. These samples were then paired with TPMS systems made from neat PLA. In the first phase of the investigation, we identified the optimal number of layers to ensure effective reinforcement while avoiding unnecessary over-reinforcement.

**Z specimens:** All standalone shells exhibited unstable failure modes.

**Table 3**
Names, structural properties, and dominant failure modes of the tested specimens.

| Samples | Base material | Orientation | Radially reinforced hoop layer count | 3D printed, axial reinforcement | Specimen type | Dominant failure mode |
|---|---|---|---|---|---|---|
| Shell 1 | Prepreg | radial | 1 | no | – | Matrix crushing (unstable) |
| Shell 2 | | radial | 2 | no | – | Matrix crushing (unstable) |
| Shell 3 | | radial | 3 | no | – | Matrix crushing (unstable) |
| PLA 1 | PLA | Z | 0 | no | Type 1 | Plastic cell collapse (stable) |
| PLA 2 | | Z | 1 | no | Type 4 | Plastic cell collapse (stable) |
| PLA 3 | | Z | 2 | no | Type 4 | Plastic cell collapse (stable) |
| PLA 4 | | Z | 3 | no | Type 4 | Plastic cell collapse (stable) |
| PLA 5 | | XY | 0 | no | Type 2 | Brittle cell collapse (unstable) |
| PLA 6 | | XY | 2 | no | Type 5 | Plastic cell collapse (stable) |
| PLA 7 | | XY | 3 | no | Type 5 | Plastic cell collapse (stable) |
| PA 1 | PA | Z | 0 | no | Type 1 | Plastic cell collapse (stable) |
| PA 2 | | Z | 3 | no | Type 4 | Plastic cell collapse (stable) |
| PA 3 | | XY | 0 | no | Type 2 | Delamination (unstable) |
| PA 4 | | XY | 3 | no | Type 5 | Plastic cell collapse (stable) |
| PA 5 | | XY | 0 | yes | Type 3 | Delamination (unstable) |
| PA 6 | | XY | 3 | yes | Type 6 | Plastic cell collapse + fragmentation (stable) |
| Onyx 1 | Onyx | Z | 0 | no | Type 1 | Plastic cell collapse (stable) |
| Onyx 2 | | Z | 3 | no | Type 4 | Plastic cell collapse (stable) |
| Onyx 3 | | XY | 0 | no | Type 2 | Delamination (unstable) |
| Onyx 4 | | XY | 3 | no | Type 5 | Plastic cell collapse (stable) |
| Onyx 5 | | XY | 0 | yes | Type 3 | Delamination (unstable) |
| Onyx 6 | | XY | 3 | yes | Type 6 | Plastic cell collapse + fragmentation (stable) |

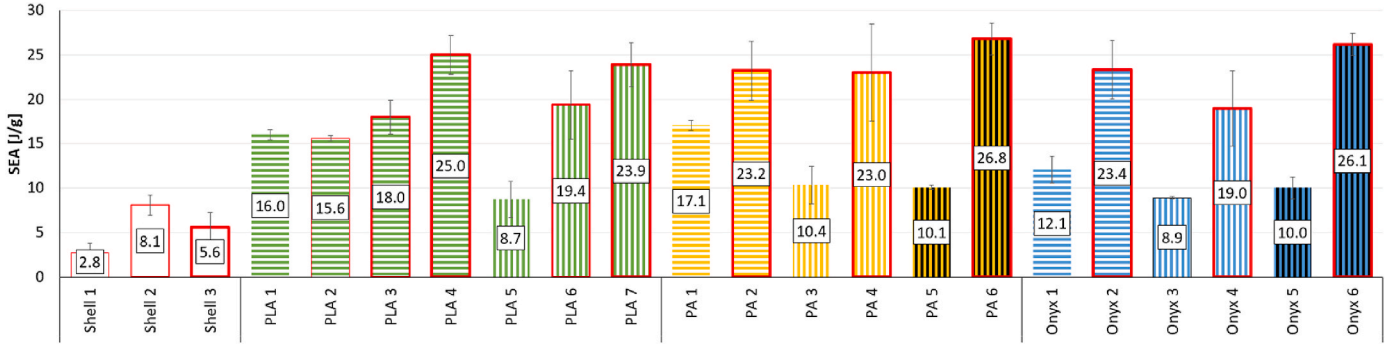


**Fig. 5.** Bar chart summarizing the SEA results of all tested structures. The columns with red outlines indicate external shell reinforcement, with line thickness proportional to the number of layers (1-2-3). The orientation of hatching represents the manufacturing orientation of the internal structure: white stripes indicate unreinforced specimens, while black lines denote axially reinforced specimens.

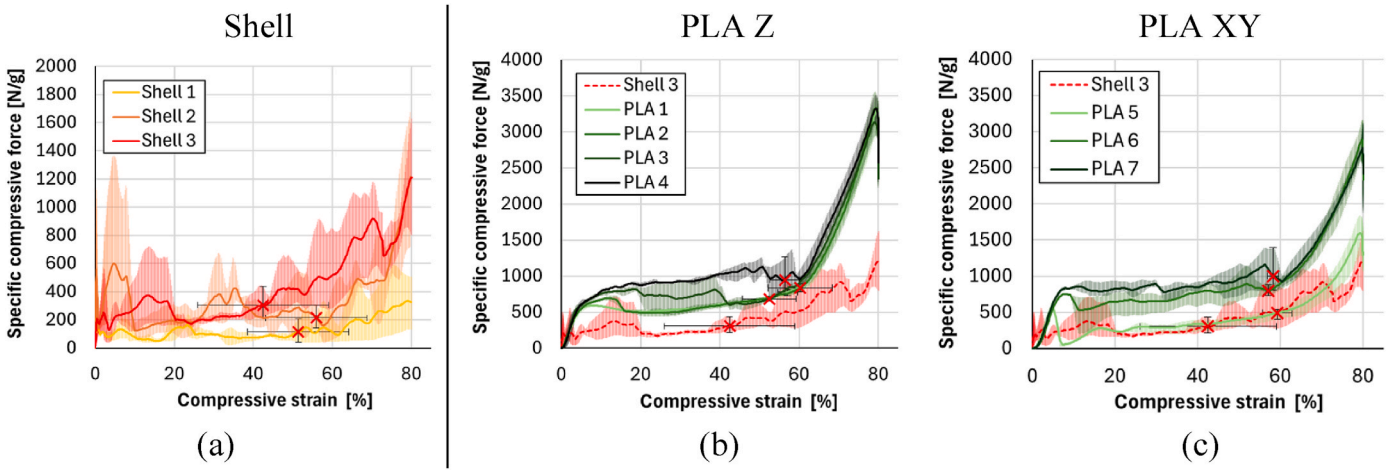


**Fig. 6.** Load–displacement curves of separately tested shell structures (a) and neat PLA cellular structures without radial reinforcement (Type 1 and Type 2 specimens) compared to radially reinforced structures (Type 4 and Type 5 specimens) with hoop layer counts between 1 and 3 in orientation Z (b) and XY (c).

**Table 4**
Performance increment achieved by CFRP shells for different specimens.

| | Samples | TPMS weight [g] | Shell weight [g] | SEA $_{TPMS,act.}$ [J/g] | SEA $_{shell,act.}$ [J/g] | SEA $_{total,\ ROM}$ [J/g] | SEA $_{total,act.}$ [J/g] | ΔSEA $_{abs.}$ [%] | Synergy $_{SEA}$ [%] |
|---|---|---|---|---|---|---|---|---|---|
| XY orientation | PLA 6 | 35.8 ± 0.5 | 5.4 ± 0.1 | 8.7 ± 2.0 | 8.1 ± 1.1 | 8.6 | 19.4 ± 3.8 | 122 ± 43 | 124 ± 21 |
| | PLA 7 | 35.6 ± 0.5 | 8.0 ± 0.2 | 8.7 ± 2.0 | 5.6 ± 1.7 | 8.1 | 23.9 ± 2.4 | 174 ± 33 | 194 ± 12 |
| | PA 4 | 41.5 ± 0.4 | 8.0 ± 0.2 | 10.4 ± 2.1 | 5.6 ± 1.7 | 9.4 | 23.0 ± 5.5 | 122 ± 44 | 144 ± 25 |
| | PA 6 | 40.4 ± 0.5 | 8.0 ± 0.2 | 10.1 ± 0.2 | 5.6 ± 1.7 | 9.6 | 26.8 ± 1.8 | 166 ± 27 | 180 ± 8 |
| | Onyx 4 | 36.2 ± 0.2 | 8.0 ± 0.2 | 8.9 ± 0.1 | 5.6 ± 1.7 | 8.2 | 19.0 ± 4.3 | 113 ± 24 | 131 ± 23 |
| | Onyx 6 | 35.0 ± 0.5 | 8.0 ± 0.2 | 10.0 ± 1.2 | 5.6 ± 1.7 | 8.7 | 26.1 ± 2.4 | 161 ± 17 | 202 ± 6 |
| Z orientation | PLA 2 | 36.0 ± 0.1 | 2.7 ± 0.04 | 16.0 ± 0.6 | 2.8 ± 1.0 | 15.0 | 15.6 ± 0.3 | −3±5 | 4 ± 3 |
| | PLA 3 | 36.0 ± 1.4 | 5.4 ± 0.1 | 16.0 ± 0.6 | 8.1 ± 1.1 | 14.7 | 18.0 ± 1.9 | 12 ± 14 | 23 ± 11 |
| | PLA 4 | 36.0 ± 0.5 | 8.0 ± 0.2 | 16.0 ± 0.6 | 5.6 ± 1.7 | 13.9 | 25.0 ± 2.2 | 56 ± 12 | 79 ± 10 |
| | PA 2 | 39.9 ± 0.4 | 8.1 ± 0.2 | 17.1 ± 0.6 | 5.6 ± 1.7 | 15.1 | 23.2 ± 3.4 | 36 ± 18 | 54 ± 16 |
| | Onyx 2 | 36.4 ± 0.2 | 8.1 ± 0.2 | 12.1 ± 1.5 | 5.6 ± 1.7 | 11.0 | 23.4 ± 3.4 | 94 ± 26 | 112 ± 15 |

Following an initial abrupt loading stage, there was a significant drop, follows by a densification stage with fluctuating amplitudes (Fig. 6 (a)). This general instability can explain the significant scatter of the densification onset points of shell structures (marked with a red X).

In the case of the radially reinforced TPMS system, a single hoop layer did not improve performance in the Z-orientation (SEA: −3 %, Synergy: 4 %). However, these values increased to 12 % and 23 % with two hoop layers, respectively, and rose to 56 % and 79 % with three. The force–displacement curves and failure modes indicated progressively more stable behavior. While the two-layer reinforced structure exhibited an abrupt drop, suggesting an unstable shell failure at this point (Fig. 7 (a)), the three-layer configuration displayed a more consistent response (Fig. 7 (b)). The additional layer extended the plateau phase of the two-layer curve (Fig. 6 (b): PLA 3), producing a quasi-ideal energy absorption characteristic with a sustained plateau and a well-defined densification point.

**XY specimens:** In the examined configuration, single-layer shell structures could not withstand radial forces throughout the entire stroke length. This led to premature failure of both the shell and the cellular core as the radial strength limit was exceeded. This failure resulted in an abrupt drop in reaction forces before the densification point was reached. In contrast, the three-layer configuration demonstrated a

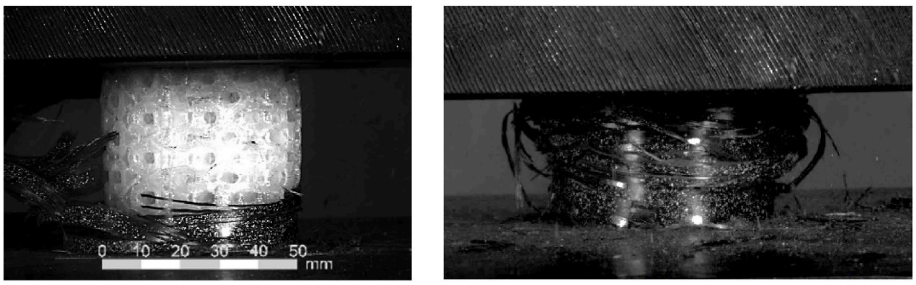


**Fig. 7.** The influence of shell strength on the failure modes: In tests on PLA printed in Z orientation with two hoop layers of reinforcement, the hoop layers snapped at 40 % deformation, making failure unstable (a). In contrast, the same specimen reinforced with three layers demonstrated stable characteristics and increased energy absorption throughout, due to the appropriate radial reinforcement (b).

progressive and predictable failure mode. Consequently, in further XY-oriented tests, we focused exclusively on two- and three-layer shell configurations. These tests showed even more pronounced improvements: the two-layer specimens exhibited a 122 % increase in SEA and a 124 % synergistic effect (Fig. 6 (c): PLA 6). In comparison, the three-layer specimens demonstrated a 174 % increase in SEA and a 194 % synergistic improvement (Fig. 6 (c): PLA 7).

The findings on the optimal number of hoop layers indicate that the radial strength of the shell structure plays a crucial role in enhancing energy absorption capacity and must be carefully matched with the mechanical properties of the cellular structure.

### 4.2. The effect of printing orientation

In our tests, the printing orientation strongly influenced the performance-enhancing effect of the hoop layers. The Z-oriented specimens exhibited an average synergistic impact of 54 % for specimens with three hoop layers, while the XY-oriented specimens demonstrated a 170 % increase. Z-type specimens exhibited superior energy absorption compared to those printed in the XY orientation. The difference was 61 % for unreinforced specimens, but it was only an average of 8 % for shell-reinforced specimens. This can be explained as follows: In the Z-oriented specimens, the printed layers were oriented transversely to the applied load, meaning that the inherent weak points associated with the layers did not play a critical role in failure progression (Fig. 8 (a)). In contrast, XY-oriented specimens exhibited premature failure due to delamination and local buckling (Fig. 8 (b)), a mode of failure which the hoop layers effectively prevented. Hoop layers enhanced energy absorption capacity in both orientations and mitigated the adverse impact of unfavorable printing orientation, resulting in nearly identical elevated SEA values (Fig. 5: PLA 4 vs. PLA 7, PA 2 vs. PA 4, Onyx 2 vs. Onyx 4).

### 4.3. The effect of the material

In this study, we investigated three distinct categories of materials: PLA (unreinforced reference), PA, and Onyx, suitable for reinforcing with continuous fibers. The synergistic effect was similar in the case of all tested materials. The PLA-based specimens had the highest absolute performance (SEA), followed by PA and Onyx. While PLA-based specimens were not included in the investigation of the axially reinforced configuration, they demonstrated that the introduced hoop layers effectively transformed the unstable, brittle failure of the cells into stable, progressive failure (Fig. 5: PLA 5 vs. PLA 7).

3D-printed fiber-reinforced PA and Onyx specimens demonstrated statistically identical properties within the margin of error (10.6 vs. 10.2 J/g). However, when external shells were applied, PA exhibited slightly higher SEA improvement, approximately 3 % higher than fiber-reinforced Onyx. In Z-oriented specimens, the behavior of PA were more similar to that of the brittle PLA than those of the more ductile Onyx. This difference can be attributed to the different plastic behavior of the two materials: while PA had higher average plateau forces, the Onyx specimens deviated from linearity sooner. This resulted in a more gradual transition between the initial loading phase and the plateau region. As a result, their average plateau forces and SEA declined compared to the PA samples (Fig. 9 (a) compared to (b), and Fig. 9 (c) compared to (d)).

### 4.4. The effect of fiber reinforcement

The results indicate that fiber reinforcement enhances the SEA of the specimens, but the contributions of axial and radial reinforcement differ

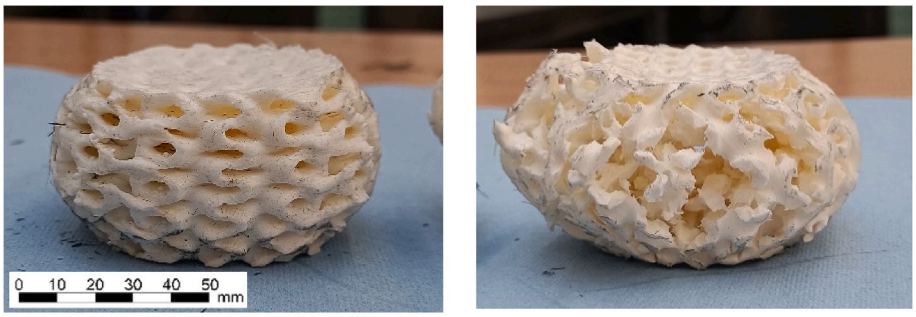


**Fig. 8.** Typical failure modes of PA and Onyx specimens printed in Z (a) and XY orientation (b). While the specimens printed in Z orientation maintained their stability over the entire deformation range, the XY specimens suffered delamination-dominated premature failure due to their weaker radial load-carrying capacity, which resulted in significantly reduced SEA.

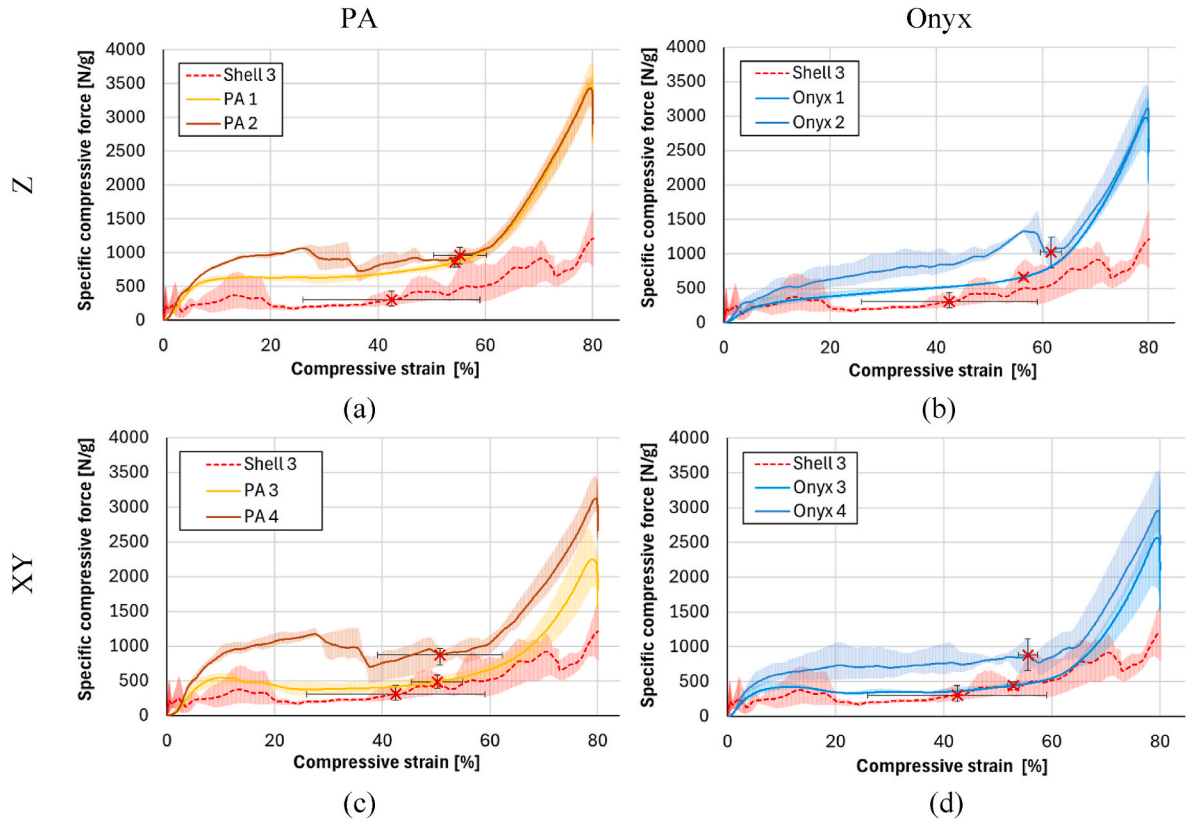


**Fig. 9.** Specific force–compressive strain curves of neat PA (a, c) and Onyx (b, d) specimens: the diagrams show compression results for individual (Type 1 and Type 2 specimens) and shell-reinforced configurations (Type 4 and Type 5 specimens).

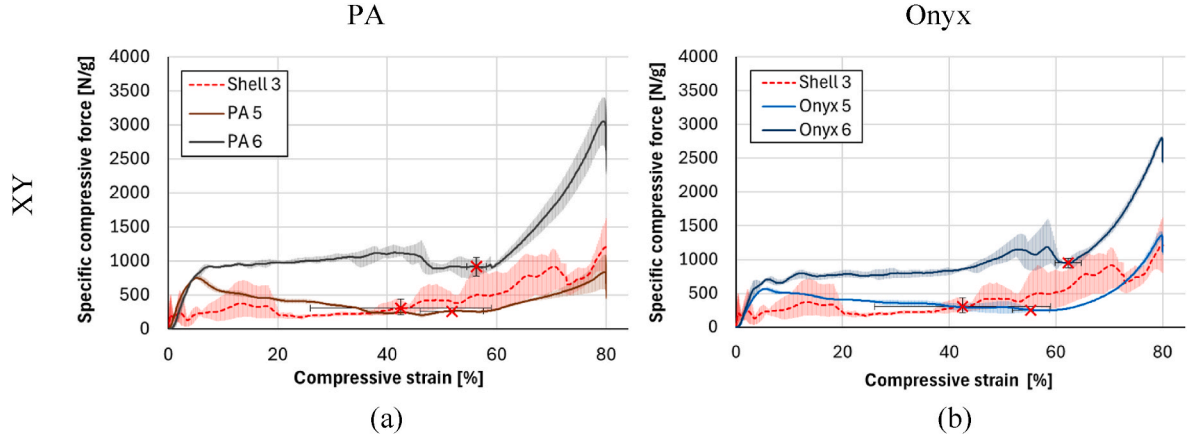


**Fig. 10.** Specific force–compressive strain curves of the tested PA (a) and Onyx-based (b) specimens with axial reinforcement (Type 3 and Type 6 specimens). The diagrams show the compression curves measured separately for individual components and combined systems, highlighting the effectiveness of the hoop layers.

significantly. In axially reinforced PA and Onyx specimens without radial reinforcement, performance remained similar to their non-reinforced counterparts (Fig. 5: PA 3 vs. PA 5; Onyx 3 vs. Onyx 5). However, when combined with radial reinforcement, the specimens exhibited the highest SEA among all tested configurations. The results in Fig. 10 show the distinct characteristics of axially reinforced specimens (PA 5 and Onyx 5 samples) and their hybrid-reinforced counterparts (PA 6 and Onyx 6 samples). The radial reinforcement increased the plateau forces in the examined setups, stabilizing the failure mode throughout the deformation range. Axially reinforced PA and Onyx specimens exhibited a more unstable behavior, characterized by a distinct local maximum after the initial quasi-linear segment (Fig. 10: PA 5 and Onyx 5), followed by a monotonic decrease in plateau forces up to the theoretical densification point. The underlying causes of these phenomena will be examined in the following sections.

#### 4.4.1. *Radial reinforcement*

Our general objective with this study was to improve the energy absorption capability of 3D-printed CFRP systems by preventing premature, delamination-driven failure modes observed in previously researched [19] fiber-reinforced TPMS structures. However, based on our initial findings, we extended our investigations to unreinforced 3D-printed structures, as weak interlayer adhesion presents a similarly significant challenge in both cases. Even axially unreinforced specimens

produced synergistic effects, suggesting that radial reinforcement can effectively stabilize 3D-printed structures against local micro- and mesoscale buckling, where weak interlayer adhesion significantly affects structural integrity. In general, specimens without radial reinforcement often exhibited significant drops and instability after the initial loading phase (Fig. 6: PLA 1, PLA 5, and Fig. 10: PA 5). On the other hand, radially reinforced structures had a stabilized response, with smaller fluctuations and a monotonically increasing trend without excessive drops in the load–displacement curve. Fig. 11 shows the effect of radial reinforcement on the failure mode and crash front of the hybrid-reinforced TPMS structure. In reinforced specimens, the failure mode was both predictable and stable, progressing vertically from one layer of cells to the next (Fig. 11 (b)). As the crash front advanced, the hoop layers fractured simultaneously, ensuring consistent radial support. SEA and synergy metrics further support this observation. For the most efficient three-layer shell configuration, performance improvements in SEA ranged from 36 % to 174 %, while synergy effects varied between 54 % and 200 %. This confirms that shell reinforcement synergistically improves the energy absorption of TPMS structures.

Based on the load–displacement curves and the visual investigation of the crushed specimens, we concluded that the increased radial strength of the hybrid structure enhances the energy absorption capacity of the cellular system through three distinct effects. On the macroscale, a reduction in the Poisson's ratio of the cell structure limits its ability to deflect under compressive loads, thereby increasing axial resistance. Additionally, the lateral integrity of the structure improves as the hoop layers constrain the cellular system during crushing, resulting in a more gradual collapse of individual cells. Lastly, when axial fiber reinforcement is present, the radial support facilitates the fragmentation of fibers into smaller segments, which also adds to the energy dissipation of the samples.

#### 4.4.2. Axial reinforcement

Axially reinforced specimens had the most significant difference between the performance of their configurations. In the case of the hybrid-reinforced specimen, SEA improved by 166 % for the PA specimens and 161 % for their Onyx counterparts (Fig. 5 and Table 4: PA 6 and Onyx 6). These results exceed the 122 % and 113 % SEA differences in the neat, unreinforced, and radially reinforced samples (Fig. 5 and Table 4: PA 4 and Onyx 4). The difference in average of 46 % can be attributed to the adequately utilized axial reinforcement. We captured microscopic images of the internal surfaces of the fragments to better understand the behavior of the samples under crushing (Fig. 12). These images, at 20× magnification, clearly show the differences in the failure modes of the axially placed fiber bundles. While the prematurely failed, delaminated specimen has longer, uninterrupted fiber segments with a few fracture points in the highlighted area (Fig. 12: (a)), fibers in the radially reinforced specimen fractured into significantly smaller segments with uniform distribution in the highlighted area (Fig. 12: (c)). Since the onset of fragmentation indicates increased energy absorption, a higher degree of fragmentation with smaller segments corresponds to greater energy absorption capacity. We assume that the onset of fragmentation was enabled by the improved support of the 3D-printed fiber strands, which reduced the unsupported buckling length encountered by the crash front. This, in turn, facilitated a more efficient fragmentation of the fibers.

The variation in SEA between axially reinforced TPMS structures and hybrid structures (with both axial and radial reinforcement) quantitatively show the effect of the initiated fragmentation mechanisms. Onyx specimens had a 12 % higher SEA in the axially reinforced configurations (Fig. 5: Onyx 3 vs. Onyx 5), while PA specimens exhibited a 3 % reduction compared to their unreinforced counterparts (Fig. 5: PA 3 vs. PA 5). Incorporating radial reinforcement resulted in a 27 % and 14 % increase in SEA, respectively (Fig. 5: Onyx 5 vs. Onyx 6 and PA 5 vs. PA 6). This suggests that the initiation of fragmentation contributes with the difference of the two datasets, between 15 % and 17 % to the energy absorption performance of the respective configurations.

### 4.5. The effect of the stroke length calculation method

In this study, SEA was evaluated using both the dynamic method, based on Equations (2), (3), and (4), and the static method, which relies on the theoretical densification point derived from relative porosity ($\epsilon_d = 0.6$). The static method provided a fixed reference, while the dynamic approach accounted for variations in deformation behavior. There was a strong correlation of 0.98 between the two datasets. The static method showed 7 % higher SEA on average and a maximum SEA deviation of 20 %. These findings confirm that the trends observed in Sections 4.1.–4.4. persist regardless of the two evaluation methods, demonstrating that shell reinforcement stabilizes the structure and enhances its load-bearing capacity.

## 5. Conclusions

In this study, carbon fiber–epoxy prepreg shells were used to enhance the energy absorption performance of TPMS specimens by mitigating premature failure modes such as delamination and local buckling. This approach was validated with quasi-dynamic compression tests on TPMS structures with and without radially reinforced CFRP shells. Specimens were fabricated from neat PLA, PA, and Onyx, with PA

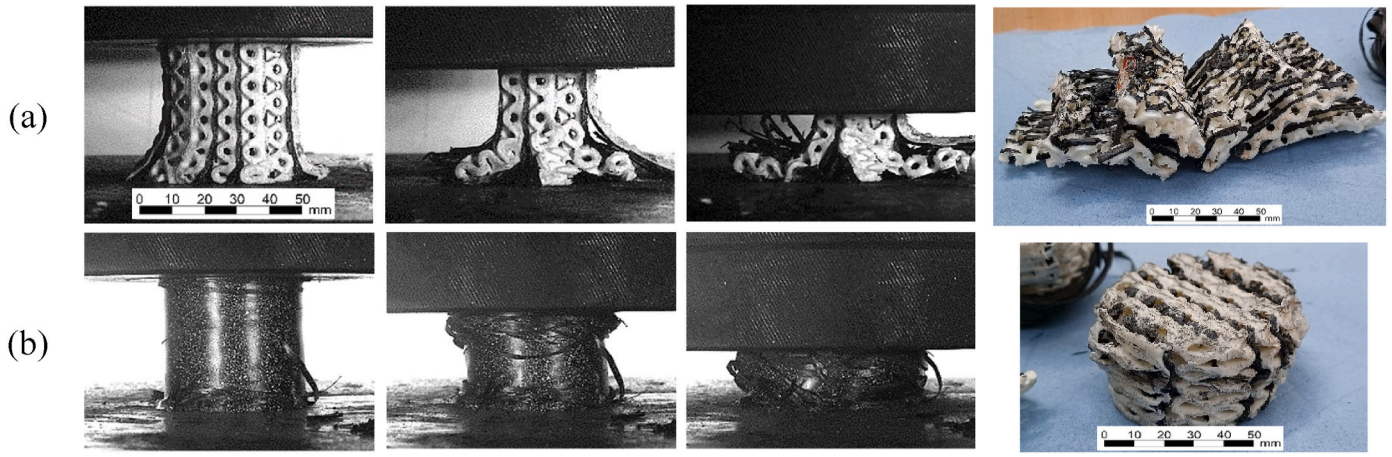


**Fig. 11.** Effect of hoop layers on the failure modes of 3D printed continuous fiber–reinforced structures. The figure shows the differences between PA 5 (a) and PA 6 (b) specimens during compression testing, where the axially reinforced structure fails prematurely through delamination, while the radially reinforced specimen holds its structural integrity.

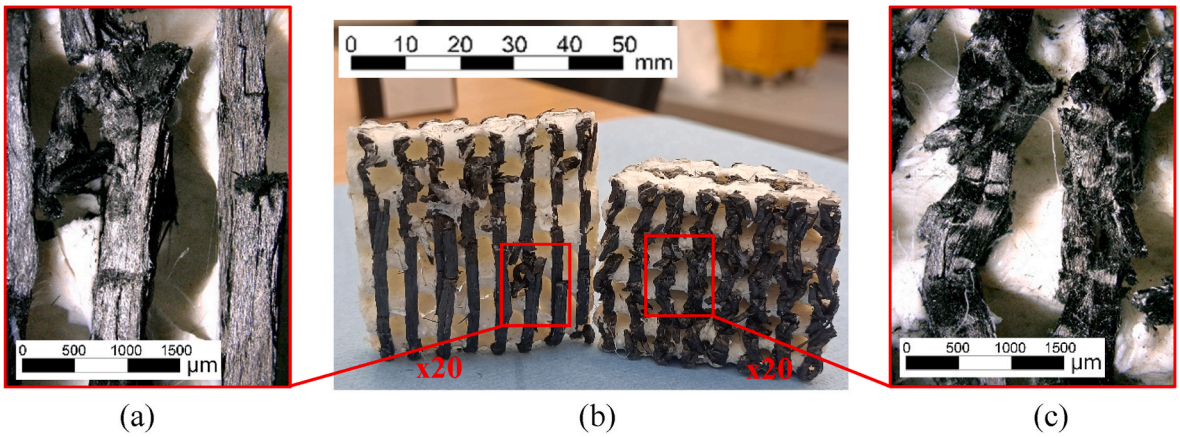


**Fig. 12.** Cross-sectional images of PA specimens with axial fiber reinforcement after crushing. The occurring fiber fragmentation (c) indicates effective failure mechanisms on the micro-level.

and Onyx incorporating continuous carbon fiber reinforcement laid axially. Adding radially reinforced shells significantly improved axial load-bearing capacity during crushing and promoted more stable failure modes with higher specific energy absorption (SEA). The key findings of this study are as follows:

- The combination of CFRP shells and fiber-reinforced TPMS structures resulted in quasi-stable failure behavior, maximizing energy absorption efficiency.
- Hoop layer–initiated fragmentation in axially reinforced specimens contributed to an average performance improvement of 16 %, enabled by reduced unsupported buckling length of the axial fibers.
- The radially reinforced CFRP shell showed a synergistic effect in energy absorption properties by an average of 136 ± 14 %, which was higher (190 ± 7 %) for fiber-reinforced specimens.
- The reinforcing effect of the hoop layers was orientation-dependent due to interlayer weaknesses from the printing process, with XY-oriented specimens showing a 169 ± 15 % increase. Z-oriented specimens showed an improvement of only 82 ± 13 %, but radial reinforcement increased SEA to similar values for both configurations.

The present study focused exclusively on the Schwarz-Diamond TPMS cell with a constant relative density of 37.3 %. It is recommended that these parameters be broadened for more robust conclusions. In the calculations, the embedded axial reinforcement was homogenized with the cellular structure instead of treating it as a distinct component. Furthermore, micro-level defects inherent to 3D-printed composites, such as porosity, geometric inaccuracies, and fiber waviness, were not considered despite their significant impact on macroscale properties. Future research should address these limitations and refine the introduced approach to directly quantify the contribution of axial reinforcement to the hybrid system.

## CRediT authorship contribution statement

**Bence Szederkényi:** Writing – review & editing, Writing – original draft, Visualization, Validation, Software, Methodology, Formal analysis, Data curation, Conceptualization. **Norbert K. Kovács:** Writing – review & editing, Writing – original draft, Supervision, Software, Methodology, Conceptualization. **Tibor Czigany:** Writing – review & editing, Writing – original draft, Validation, Supervision, Methodology, Funding acquisition, Conceptualization.

## Declaration of competing interest

The authors declare that they have no known competing financial interests or personal relationships that could have appeared to influence the work reported in this paper.

## Acknowledgments

The research reported in this paper was supported by the National Research, Development, and Innovation Office (NRDI, Hungary) through grants OTKA K 146236 and OTKA K 138472.

The authors acknowledge the Ministry of Culture and Innovation of Hungary for support from the National Research, Development and Innovation Fund through grant no. NKKP ADVANCED 149578.

Project no. TKP-6-6/PALY-2021 has been implemented with the support provided by the Ministry of Culture and Innovation of Hungary from the National Research, Development and Innovation Fund, financed under the TKP2021-NVA funding scheme.

The project 2022–2.1.1-NL-2022-00012 has been implemented with the support provided by the Ministry of Culture and Innovation of Hungary from the National Research, Development and Innovation Fund, financed under the 2022–2.1.1-NL Creation of National Laboratories, Complex Development funding scheme.

Bence Szederkényi expresses appreciation for the support of the Doctoral Excellence Fellowship Programme (DCEP) and of the University Research Fellowship Programme (EKÖP) funded by the National Research Development and Innovation Fund of the Ministry of Culture and Innovation and the Budapest University of Technology and Economics, under a grant agreement with the National Research, Development and Innovation Office.

Norbert Krisztián Kovács expresses appreciation for the support of the János Bolyai Research Scholarship of the Hungarian Academy of Sciences.

## Data availability

Data will be made available on request.

## References

[1] Lu G, Yu T. Consequences of vehicle accidents. In: Energy absorpt. Struct. Mater. Boca Raton: CRC Press; 2003. p. 4–6.
[2] Lu G, Yu T. Human body's tolerance to impact. In: Energy absorpt. Struct. Mater. Boca Raton: CRC Press; 2003. p. 7–10.
[3] Tomin M, Kmetty Á. Polymer foams as advanced energy absorbing materials for sports applications—a review. J Appl Polym Sci 2022;139:1–23. https://doi.org/10.1002/app.51714.

[4] Orbulov IN, Szlancsik A, Kemény A, Kincses D. Low-cost light-weight composite metal foams for transportation applications. J Mater Eng Perform 2022;31:6954–61. https://doi.org/10.1007/s11665-022-06644-4.
[5] Starbuck JM, Adams DO, Courteau M. Energy absorbing damage mechanisms in progressive crushing of composite tubes. In: 32nd tech conf Am soc compos 2017, vol. 2; 2017. p. 1419–32. https://doi.org/10.12783/asc2017/15279.
[6] Heimbs S, Strobl F. Crash simulation of an F1 racing car front impact structure. 7th Eur. LS-DYNA Conf. 2009:1–8.
[7] Boria S, Obradovic J, Belingardi G. Experimental and numerical investigations of the impact behaviour of composite frontal crash structures. Compos Part B Eng 2015;79:20–7. https://doi.org/10.1016/j.compositesb.2015.04.016.
[8] Kohlgrueber D, Kamoulakos A. Validation of numerical simulation of composite helicopter sub-floor structures under crash loading. In: Am. Helicopter soc. 54th annu. Forum by Am. Helicopter soc. Inc.; 1998. p. 10. Washington, DC.
[9] Abueidda DW, Bakir M, Abu Al-Rub RK, Bergström JS, Sobh NA, Jasiuk I. Mechanical properties of 3D printed polymeric cellular materials with triply periodic minimal surface architectures. Mater Des 2017;122:255–67. https://doi.org/10.1016/j.matdes.2017.03.018.
[10] Abueidda DW, Elhebeary M, Shiang Cs Andrew, Pang S, Abu Al-Rub RK, Jasiuk IM. Mechanical properties of 3D printed polymeric Gyroid cellular structures: experimental and finite element study. Mater Des 2019;165:107597. https://doi.org/10.1016/j.matdes.2019.107597.
[11] Sood M, Wu CM. Influence of 3D printed structures on energy absorption ability of brittle polymers under dynamic cyclic loading. Express Polym Lett 2023;17:390–405. https://doi.org/10.3144/expresspolymlett.2023.28.
[12] Kladovasilakis N, Tsongas K, Kostavelis I, Tzovaras D, Tzetzis D. Effective mechanical properties of additive manufactured triply periodic minimal surfaces: experimental and finite element study. Int J Adv Manuf Technol 2022;121:7169–89. https://doi.org/10.1007/s00170-022-09651-w.
[13] Sathishkumar N, Arunkumar N, Rohith SV, Hariharan RR. Effect of varying unit cell size on energy absorption behaviour of additive manufactured TPMS PETG lattice structure. Prog Addit Manuf 2023;8:1379–91. https://doi.org/10.1007/s40964-023-00407-w.
[14] Qiu N, Zhang J, Li C, Shen Y, Fang J. Mechanical properties of three-dimensional functionally graded triply periodic minimum surface structures. Int J Mech Sci 2023;246:108118. https://doi.org/10.1016/j.ijmecsci.2023.108118.
[15] Santiago R, Ramos H, AlMahri S, Banabila O, Alabdouli H, Lee DW, et al. Modelling and optimisation of TPMS-based lattices subjected to high strain-rate impact loadings. Int J Impact Eng 2023;177:104592. https://doi.org/10.1016/j.ijimpeng.2023.104592.
[16] Alduais A, Özerinç S. Tunable mechanical properties of thermoplastic foams produced by additive manufacturing. Express Polym Lett 2023;17:317–33. https://doi.org/10.3144/expresspolymlett.2023.23.
[17] Bhudolia SK, Gohel G, Subramanyam ESB, Leong KF, Gerard P. Enhanced impact energy absorption and failure characteristics of novel fully thermoplastic and hybrid composite bicycle helmet shells. Mater Des 2021;209:110003. https://doi.org/10.1016/j.matdes.2021.110003.
[18] Zhu G, Sun G, Yu H, Li S, Li Q. Energy absorption of metal, composite and metal/composite hybrid structures under oblique crushing loading. Int J Mech Sci 2018;135:458–83. https://doi.org/10.1016/j.ijmecsci.2017.11.017.
[19] Szederkényi B, Krisztián Kovács N, Czigány T. Investigation of continuous fiber–Rreinforced triply periodic minimal surfaces (TPMS) for high-performance energy absorption applications. Proc. 21st Eur. Conf. Compos. Mater 2024:1651–8.
[20] Saleh M, Anwar S, Al-Ahmari AM, Alfaify A. Compression performance and failure analysis of 3D-printed carbon fiber/PLA composite TPMS lattice structures. Polymers (Basel) 2022;14:4595. https://doi.org/10.3390/polym14214595.
[21] Lupone F, Padovano E, Venezia C, Badini C. Experimental characterization and modeling of 3D printed continuous carbon fibers composites with different fiber orientation produced by FFF process. Polymers (Basel) 2022;14. https://doi.org/10.3390/polym14030426.
[22] Zhang X, Xie X, Li Y, Li B, Yan S, Wen P. Mechanical behavior of Al-Si10-Mg P-TPMS structure fabricated by selective laser melting and a unified mathematical model with geometrical parameter. Materials (Basel) 2023;16. https://doi.org/10.3390/ma16020468.